Journal of Materials Chemistry C

Structure-property trends in a hollandite multiferroic by Fe doping: structural, magnetic and dielectric characterization of nanocrystalline $BaMn_{3-x}Fe_xTi_4O_{14+\delta}$

Journal:	*Journal of Materials Chemistry C*
Manuscript ID	TC-ART-02-2020-000703.R1
Article Type:	Paper
Date Submitted by the Author:	01-May-2020
Complete List of Authors:	Pearsall, Frederick; City College of New York, Chemistry Farahmand, Nasim; The Graduate Center of the City University of New York, Ph.D. Program in Chemistry; The City College of New York, Chemistry and BIochemistry Lombardi, Julien; City College of New York, Chemistry, Dehipawala, Sunil ; Queensborough Community College, Department of Physics Gai, Zheng; Oak Ridge National Laboratory, CNMS O'Brien, Stephen; City College of New York, Chemistry

Structure-property trends in a hollandite multiferroic by Fe doping: structural, magnetic and dielectric characterization of nanocrystalline $BaMn_{3-x}Fe_xTi_4O_{14+\delta}$

Frederick Pearsall,[a,b,c] Nasim Farahmand, [a,b,c] Julien Lombardi[a,b,c], Sunil Dehipawala[d], Zheng Gai[e] and Stephen O'Brien[a,b,c*]

[a]The CUNY Energy Institute, City University of New York, Steinman Hall, 160 Convent Avenue, The City College of New York, New York, NY 10031, USA.

[b]Department of Chemistry, The City College of New York, 1024 Marshak, 160 Convent Avenue, NY 10031, USA

[c] Ph.D. Program in Chemistry, The Graduate Center of the City University of New York, New York, NY 10016, USA.

[d]Department of Physics, Queensborough Community College, 222-05 56th Ave, Bayside, New York, NY 11364, USA

[e]Center for Nanophase Materials Sciences and Chemical Science Division, Oak Ridge National Laboratory, Oak Ridge, TN 37831, USA

Keywords: multiferroic, nanoscale, Mossbauer spectroscopy, magnetic, dielectric

ABSTRACT: $BaMn_3Ti_4O_{14+\delta}$ (δ = 0.25, BMT-134), a recently discovered single-phase multiferroic complex oxide was doped with varying concentrations of Fe in order to assess the effect on magnetic and dielectric behavior. The novel compound $BaMn_{3-x}Fe_xTi_4O_{14+\delta}$ (BMFT) was prepared via a sol-gel chemical solution processing method. Four substituted variations were synthesized: $BaMn_{3-x}Fe_xTi_4O_{14+\delta}$ (BMFT) with x = 1, 1.5, 2, and 2.25. The approach afforded a nanocrystalline product, with control over structure and morphology, while successfully allowing increasing amounts of iron to be incorporated into the structure. All variants belong to the same hollandite *I4/m* crystal class as the parent compound, confirmed by powder XRD. Electron microscopy (TEM, EDS and SEM) provided characterization of the microstructure and elemental composition. Mossbauer spectroscopy was used to probe the local chemical environment of Fe present within the nanocrystals, to indicate oxidation state and bonding geometry. The BMFT material system was characterized as a function of temperature and applied magnetic field: M-T and M-H curves were obtained (by MPMS) and allowed the determination of Curie/Weiss constants through fitting and low temperature hysteresis

respectively. The Weiss constant becomes increasingly positive as Fe is added until an observed inflection point, indicative of an antiferromagnetic to paramagnetic short-range interaction transition. The frequency dependent dielectric permittivity of the series of BMFT compounds with differing Fe concentration, was obtained on MIM structures prepared from pressed pellets with a nanostructured morphology. The results show how Fe concentration can strongly influence dielectric behavior. Dielectric constants ranging from 100 – 1600 (low frequencies) to 150-200 (high frequencies) were observed, together with a decrease in the AC conductivity with increasing Fe.

1. Introduction

Intrinsic multiferroics are materials combining the order parameters of ferroelectricity and ferromagnetism (including antiferromagnetism), in the same phase,[1] with potential applications ranging from sensors, non-volatile memory, 4-state logic, spintronics.[1–3] Combined with materials theory, pursuing new synthetic approaches to intrinsic multiferroics can attempt to relax such restrictions on the co-existence of ions that give rise to combined polarization and magnetization.[2] The outcome of such research may not strictly produce multiferroics, but rather widen the search to, e.g. oxides with combined magnetic and dielectric properties. It has been shown that control over crystal growth, morphology, atomic architecture and defect chemistry,[4] as well as domain size control are key elements in enhancing structure-property relationships.[5] These observations point to the important role nanoscale science and engineering can play. But, initially, there is cause for concern as to whether preparing nanoscale samples will yield any promising results, due to the critical size suppression of both ferroic parameters. While suppression of the magnitude of ferroelectric polarization is observed in perovskites at the nanoscale, there is strong evidence to support the retention of off-center Ti distortions down to 5 nm, that can be the source of switchable dipoles, and ultimately ferroelectricity.[6–10] Second, the field of nanomagnetism has flourished, due in part to the increasing sensitivity of the techniques developed for magnetic property- structure relationships.[11–13] Third, nanoscale grains can be further processed to generate textured films or used in conjunction with polymers or other media to create nanocomposites, and the grain boundary effects may serve to enhance certain physical properties. In conjunction with the global drive towards miniaturization of electronic devices, it can be considered of great consequence to pursue the development of compounds that combine potential magnetization and polarization, using processes that yield nanoscale morphologies.[14] Chemical solution processing techniques offer multiple degrees of freedom in terms of doping, control over nucleation and growth (to control nanoscale morphology), and how

the final product is chemically tailored (e.g. as a colloidal dispersion). It can also offer potentially low thermal budget benchtop approaches for greener, low-cost and scalable procedures towards manufacturability. Additionally, physical deposition requires targets for the initial source of the elements or oxides, and chemical synthesis methods can provide opportunities for making targets. With the goal of ferroic materials development in mind, we engaged in preparing novel compounds based upon Ba-Ti-Mn-Fe-O compositions.

Hollandite mineral oxides, of the general formula $Ba(Mn^{4+}, Mn^{3+})O_{16}$, possess a channel like structure and lower symmetry (I/2m) to that of perovskites.[15] Until recently there were only theoretical predictions of ferroelectricity, later confirmed in BMT, $BaMn_3Ti_4O_{14.25}$.[16–18] Despite the commonplace existence of these elements in the earth's crust, a hollandite mineral containing Ba-Mn-Ti-O was not previously documented, and found to closely resemble the Redledgeite structure. Redledgeite is a rare mineral belonging to the hollandite group with the composition $Ba_xCr_{2x}Ti_{8-2x}O_{16}$, and was named for the mine it came from, the Red Ledge Mine of the Sierra Nevada mountains, CA. Redledgeite has a framework of Ti_8O_{16} octahedra with [0,0,*z*] and [½,½,*z*] channels containing Ba^{2+}.[19] It has been interpreted that the channel structure can more readily permit ion substitution with other transition metals: hollandite is essentially a more porous, flexible and lower symmetry structure than the perovskite counterpart.[20,21] It can be imagined therefore, that A^{II}-B^{IV}-O combinations that might form the perovskites may divagate towards a hollandite variations when subjected to conditions of forced substitution in which the B ion can range between charge II – IV. In this work we utilize a specialized sol-gel method called gel collection to allow for the combination of d^0 and d^n ions within the same preliminary architecture, that through low temperature, precursor driven synthesis, enables the generation of metastable states, and the arrival at stable compounds that would not necessarily have been achieved using traditional, higher temperature solid-state synthesis methods.[22–26] We targeted Mn replacement with Fe in the BMT hollandite structure sequentially to produce $BaMn_{3-x}Fe_xTi_4O_{14+\delta}$ (BMFT) with x = 1,1.5, 2, and 2.25.

2. Experimental

Nanoparticles were synthesized using the sol-gel based method (gel-collection) reported previously, which has proven to be a useful approach for the synthesis of nanocrystalline transition metal oxides. Gel-collection is an inorganic precursor driven technique that builds upon sol-gel,[27] nucleation/growth mediated nanocrystal synthesis,[28] and non-hydrolytic approaches.[29] The gel-collection approach has been reported in some detail, including chemical pathway diagrams, stepwise selection of chemical precursors, procedure and

parameters.[16,22,25,30–32] A high level of control over stoichiometry is attained due to the complete consumption of precursors during reaction to insure a high level of product fidelity. The precursors were barium isopropoxide, manganese(II) acetylacetonate, iron(II) acetylacetonate and titanium isopropoxide (Sigma Aldrich). Product stoichiometry was controlled by dissolving the precursors in 200-proof EtOH solvent in the desired molar ratio. Sol-gel transformation is performed in the anhydrous alcohol solvent by first inducing the metal alkoxides/coordination complexes to react together, prior to the stoichiometric addition of ultrapure water (18.2 MW), under inert atmospheres (Ar/N_2) and in the stark absence of surfactants and stabilizers. Under a static condition, hydrolysis of the metal alkoxides creates a gel-monolith of as-synthesized nanoparticles that in the transparent sol, of nearly 100% yield for easy separation/purification. The molar content of Mn:Fe was varied according to target stoichiometry. In a typical reaction, for example, in the synthesis of $BaMnFe_2Ti_4O_{14+\delta}$ the molar iron content in the precursor solution was twice as much as the manganese and barium molar content. 1 mmol barium isopropoxide was combined with 2 mmol manganese(II) acetylacetonate, iron(II) acetylacetonate and 4 mmol titanium isopropoxide. A 10 mL solution of 2.5 mL deionized H_2O (4% DI water of total volume) and 7.5 mL 200 proof ethanol was prepared and added dropwise to the solution under stirring leading to form a black gel. Ultrapure H_2O (18.2 MW) is used. Afterwards the solution is autoclaved at 180˚C for 48 hours, the brown gel monoloith is observed to shrink in size. The result is a gel-rod (Figure S1). Finally, the gel-rod is slowly heated to 800°C in a furnace to crystallize the product, forming a nanocrystalline powder.

Powder X-ray diffraction patterns for each variant were obtained using a PAN'alytical X-ray diffractometer with Cu Kα radiation. The average size of the particles was determined using a JEOL2100 transmission electron microscope. Energy dispersive X-ray spectroscopy (EDS) was used for elemental analysis mapping and to determine the product and precursor ratio fidelity. For electrical characterization, the compounds were pressed into pellets at 20MPa and annealed at 1000°C (8 hrs), using a Cyky 12T laboratory manual powder metallurgy press machine. The pellets were used to fabricate metal-insulator-metal (MIM) capacitors. Silver epoxy (80% conductive material) was mixed onto a glass substrate whereupon the pellets were then placed. Finally, an upper layer of silver epoxy was placed on top of the pellet, forming the second metal contact. The capacitance and dielectric loss of the pellets were measured within the frequency range of 100Hz – 2MHz, using an Agilent 4294A Precision Impedance Analyzer.

Mossbauer spectra were collected using the See-Co model W-302 spectrometer in transmission mode with Co57 source in Rh matrix. Iron oxidation state and room temperature magnetic

ordering of the BMFT compounds were obtained. A quantitative ratio of octahedral to tetrahedral coordinated iron within the materials was also obtained. M-T field-cooling (FC) and zero field-cooling (ZFC) curves at fixed applied magnetic field and M-H curves at fixed temperature were obtained. Magnetic measurements for this research were conducted at the Center for Nanophase Materials Sciences, which is a DOE office of Science User Facility. MPMS was done using a Quantum Design MPMS at Oak Ridge National Lab, Oak Ridge, TN. MPMS gives low to room temperature magnetic information. Curie-Weiss fits were obtained for all compounds.

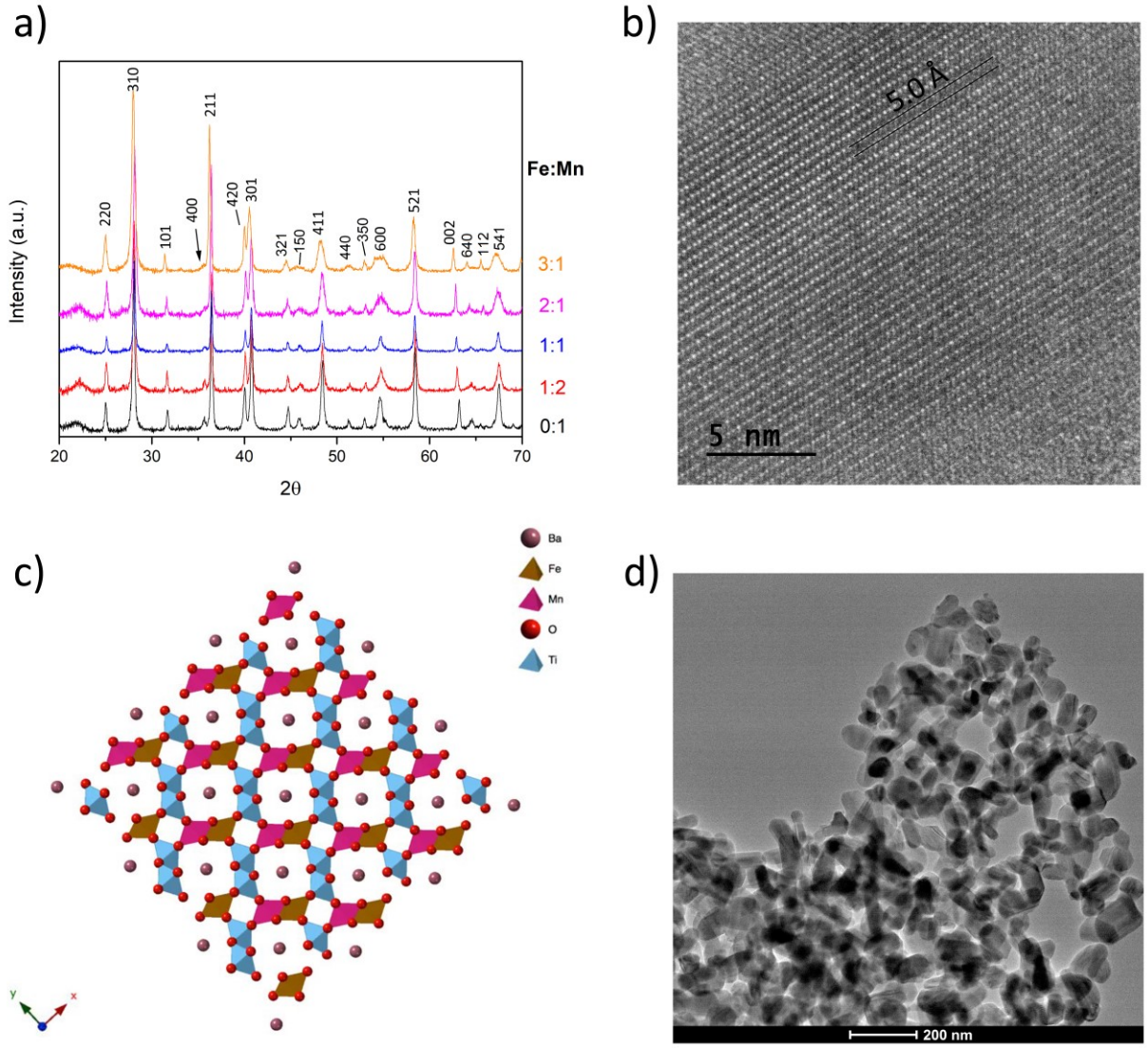

Fig. 1. a) XRD pattern comparisons of BMFT variants. The indexed peaks correspond to the main Bragg

reflections of the parent hollandite phase, as determined from a simulated powder pattern (Vesta ver. 3.4.7) based upon Space group *I4/m*, lattice parameters *a*=10.334 Å; *c*=2.903 Å. The additional peaks also belong to the same phase. b) TEM micrograph of BMFT, showing a lattice fringes. c) The hollandite crystal structure viewed along the c-axis. d) TEM of BMFT micrograph showing nanocrystal morphology.

3. Results and Discussion

In total, four stoichiometric products of BMFT were synthesized along with the parent compound; $BaMn_3Ti_4O_{14+\delta}$, $BaMn_2FeTi_4O_{14+\delta}$, $BaMn_{1.5}Fe_{1.5}Ti_4O_{14+\delta}$ and $BaMnFe_2Ti_4O_{14+\delta}$, and $BaMn_{0.75}Fe_{2.25}Ti_4O_{14+\delta}$. The compounds can be referred to by their Fe:Mn ratios, for example BMFT – 1:2, where the product is $BaMn_2FeTi_4O_{14+\delta}$, or BMFT – 1:1 where the product is $BaMn_{1.5}Fe_{1.5}Ti_4O_{14+\delta}$. While the precise value of δ is hard to fully determine, the approximate value is 0.25, which is the value ascribed to a charge neutral compound for which Mn(III) and Mn(IV) exist in equal amounts. This initially slightly odd looking stoichiometry is based upon compelling evidence (XPS and magnetic) of the existence of Mn^{3+}/Mn^{4+} within $BaMn_3Ti_4O_{14.25}$ in a 1:1 ratio.[16] It is quite typical to refine transition metal complex oxides to non-integer decimal numbers of oxygen when the oxidation state of the transition metal, such as Mn, is variable.[33]

Based upon structural characterization of the final product, Fe substitution was successful in the gel network at near room temperature (~60 ºC), but additional hydrothermal and thermal processing is required in order to acquire a fully crystallized nanomaterial of the type $BaMn_xFe_yTi_4O_{14+\delta}$. Temperatures in the range 600-800 ºC, are sufficient to produce a fully crystallized nanoceramic material, promoting M-O-M bond condensation to form a cation (e.g. Ba^{2+}) stabilized network of corner or edge sharing octahedra MO_6^{n-}. Residual organic groups are also removed from the system during this processing step. Previously BMT-134 was observed to be ferroelectric at room temperature with frequency dependent remnant polarizations of 0.02 and 0.04 C/m^2 at 50 and 500 Hz respectively, and a P-E hysteresis loop at those same frequencies, dependent on processing conditions.[17] The room temperature ferroelectricity of the compound can be forcefully elicited with the application of large external electric fields. In addition, evidence of an antiferromagnetic transition was observed, with a Néel temperature of 120 K with an average effective magnetic moment per Mn atom of 4.4 μ_B.[16] Here, we observe that replacement of manganese by iron does not appear to change the crystal structure. Energy dispersive X-ray spectroscopy (EDS) was used to determine elemental composition and to measure precursor/product ratio fidelity, which was found to be extremely high; the final composition matched well to that of the precursor ratio used during synthesis.

BMFT nanocrystals are relatively uniform in size, however, they are non-uniform in shape. Generally, they have an aspect ratio > 1 with a width and length of 50 nm and 150 nm respectively. The dependence of temperature on magnetization and the low temperature magnetic hysteresis of the compounds were observed with M-T and M-H curves obtained via MPMS. The work was performed at Oak Ridge National Lab, Center for Nanophase Materials Science. The iron containing compounds were found to have a hysteresis at 5 K. Increasing iron content gave rise to asymmetric hysteresis loops indicative of competing magnetic interactions at low temperature. An inflection point was observed at a certain threshold of iron whereupon trends in remnant magnetization and coercivity were reversed.

The family of BMT/BMFT compounds exhibited higher than expected permittivity values. Pellets with grain sizes between 100-300 nm produced high dielectric values, in the range 300-1600. Producing high dielectric constants is interesting from the perspective of energy storage applications but must be regulated with an understanding of the origins of the dielectric behavior, and how it would translate to a functional device. A comprehensive impedance spectroscopy analysis of the samples was conducted, together with modeling, in order to reach valid conclusions as to the origin of contributions to the dielectric behavior as a function of frequency.

3.1 Structural Characterization

The structure of BMFT was determined by powder X-ray diffraction (Fig. 1a) to be identical, in terms of Bragg reflections, to the BMT structure that was previously solved by pair distribution function (PDF) analysis.[16] Using Vesta Version 3.4.7,[https://jp-minerals.org/vesta] a powder pattern simulation was generated based upon the parameters obtained from the PDF data for BMT-134, with space group *I4/m*, lattice parameters *a*=10.334 Å; *c*=2.903 Å. Table 1 gives further data, atomic coordinates and anisotropic atom displacement parameters $U_{ij,}$ obtained from this prior PDF analysis, and from which the model was built. All observable peaks can be labelled according to the Bragg reflections belonging to this XRD powder pattern and are shown in Fig. 1. A slight broad peak at around 2θ =22° is also observed and attributed to trace residual amorphous material, but otherwise the samples can be declared phase pure with only one crystalline phase present. The set of Fe-substituted compounds clearly belong to the same structure as BMT-134, of the hollandite group (Fig. 1(c)). It is concluded that the BMFT ($BaMn_{3-x}Fe_xTi_4O_{14+\delta}$) set of nanocrystalline compounds closely resemble the Redledgeite structure,[34–36] also ascribed to BMT ($BaMn_3Ti_4O_{14+\delta,}$ δ=0.25). Redledgeite is a rare mineral belonging to the hollandite group with the composition $Ba_xCr_{2x}Ti_{8-2x}O_{16}$. Single crystals of Redledgeite have been

refined to the tetragonal space group *I4/m* and also to the mono-clinic space group *I2/m*, which is closely tied to the tetragonal.[19,37] One of the distinguishing features is the large size of lattice parameter *a* (~ 10.15 Å) compared to *c* (~ 2.95 Å). The majority of the Ba atoms in Redledgeite are located at the Ba_1 site at [0,0,0] and [½,½,½]. The short *c*-dimension prohibits occupancy of adjacent sites along [0,0,*z*] and [½,½,*z*], placing a constraint on the site occupancy and a limitation on cation substitution. In the case of cation substitution in BMT-134, however, placement of Fe cations within the framework is concluded to be successful for the stoichiometries attempted. Upon substitution with Fe, the Bragg reflections are observed to shift slightly towards smaller values of 2θ. There appears to be an overall trend in this direction within margins of experimental error. The shift in 2θ approximately corresponds to a small increase of the unit cell with increasing amounts of Fe. In the case of maximum Fe substitution (3:1 BMFT) the *c* parameter changes from 2.903 to approximately 2.911 Å, and the *a* parameter changes from 10.334 to approximately 10.359 Å, based upon measured shifts in the indexed Bragg reflections (e.g. d_{002}, d_{600}). Additional discussion is provided in the Supplementary information. The strong similarity in powder spectra was somewhat expected, given the closeness of values of ionic radii for Mn^{3+}, Mn^{4+} and Fe^{3+}. Textbook data for crystal ionic radii of the Mn/Fe ions shows that a substitution is geometrically feasible in the lattice (Mn(III), 72 (LS), 78.5 (HS), Mn(IV) 67 (LS), Fe(II), 75(LS), 92(HS); Fe(III), 69 (LS); 78.5(HS), Fe(IV), 72.5 values in pm, Shannon ionic radii), when comparing six-coordinated metal atoms. Tetrahedrally coordinated Fe^{3+} does have an ionic radius potentially 20% smaller than that of Mn octahedra.

Atom	x	y	z	U_{11}	U_{22}	U_{33}
Ba_1	0.5	0.5	0.976294	0.0173	0.0173	0.2729
Ba_2	0.0	0.0	0.47759	0.0193	0.0193	0.2688
O_1	0.158878	0.215003	0.005052	0.0022	0.0022	0.0056
O_2	0.166275	0.455281	0.989219	0.0030	0.0011	0.0058
Ti, Mn	0.35017	0.170772	0.990949	0.0066	0.0068	0.0182

Table 1. Crystal data for the parent compound $BaMn_3Ti_4O_{14.25}$ (BMT-134). Atomic coordinates and anisotropic atomic displacement parameters U_{ij}. Space group *I4/m*, lattice parameters *a*=10.334 Å; *c*=2.903 Å.

Fig 1. (b) and (d) show typical TEM micrographs of the BMFT series, displaying high crystallinity (see also supplementary Fig. S3), and a platelet morphology, approximately 50 nm in width and 150 nm. We conclude that the precursor driven solution processing technique directs the synthesis towards an architecture that can accommodate Fe cations, and that the use of Fe-acetylacetonate precursors, causes the direction to be towards the hollandite *I4/m* family, (as opposed to perovskites, typical of precursors used to form $BaTiO_3$).

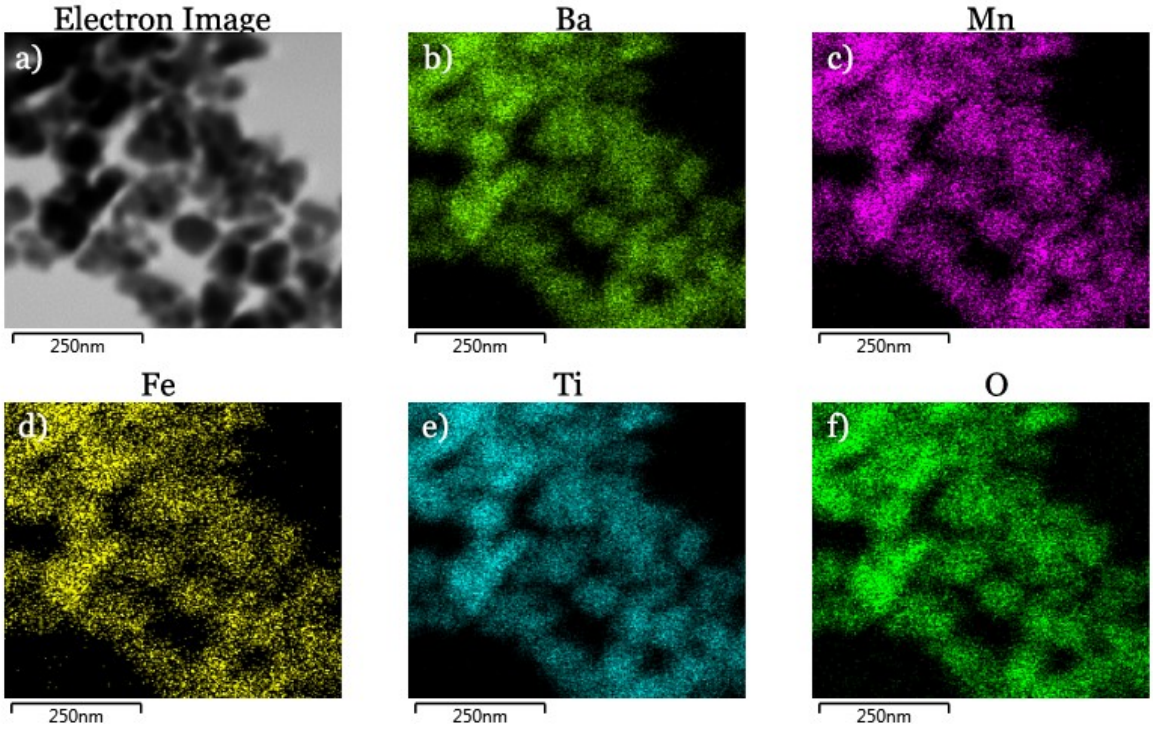

Fig. 2. Energy dispersive X-ray spectroscopy (EDS) mapping of a) electron image, b) Ba, c) Mn, d) Fe, e) Ti and f) O.

Energy dispersive X-ray spectroscopy (EDS) was performed to confirm the presence of Fe and to give an approximation of the increasing Fe:Mn ratio with increasing amounts of Fe used in the synthesis in each case. The EDS (Fig. 2) supports the assertion that Fe has successfully substituted into the lattice with retention of the hollandite crystal structure. Although one cannot assume that the final product will retain the same molar ratio, complete consumption of the precursors during reaction and the observation of a single phase at the end, is provisional evidence for deducing the product phase composition to be closely related to the initial molar

ratio of reactants. The gel-collection synthesis method has been shown to be reliable regarding retention of stoichiometry in stable perovskite compounds, including $BaTiO_3$ and derivatives, based upon accurately measured initial molar precursor concentrations.[24] Analysis of the EDS data for the series of BMFT compounds (Table S1) shows an increase in atomic % Fe for each sample, and calculations in each case serve to support the predicted Fe:Mn ratios. Mossbauer spectroscopy was used as an additional tool for a deeper analysis of the Fe sites in the structure (Fig. 3), to determine oxidation state and review any evidence of room temperature magnetic ordering. Isomer shift (IS) and quadrupole splitting (QS) can be used to determine oxidation state and the magnetic properties of the material, respectively (QS can also help determine oxidation state).[38] Table 2 displays the values for Fe oxidation state and O_h:T_d ratios for all Fe containing compounds. Peak fitting IS and QS values were obtained using an iron foil reference.

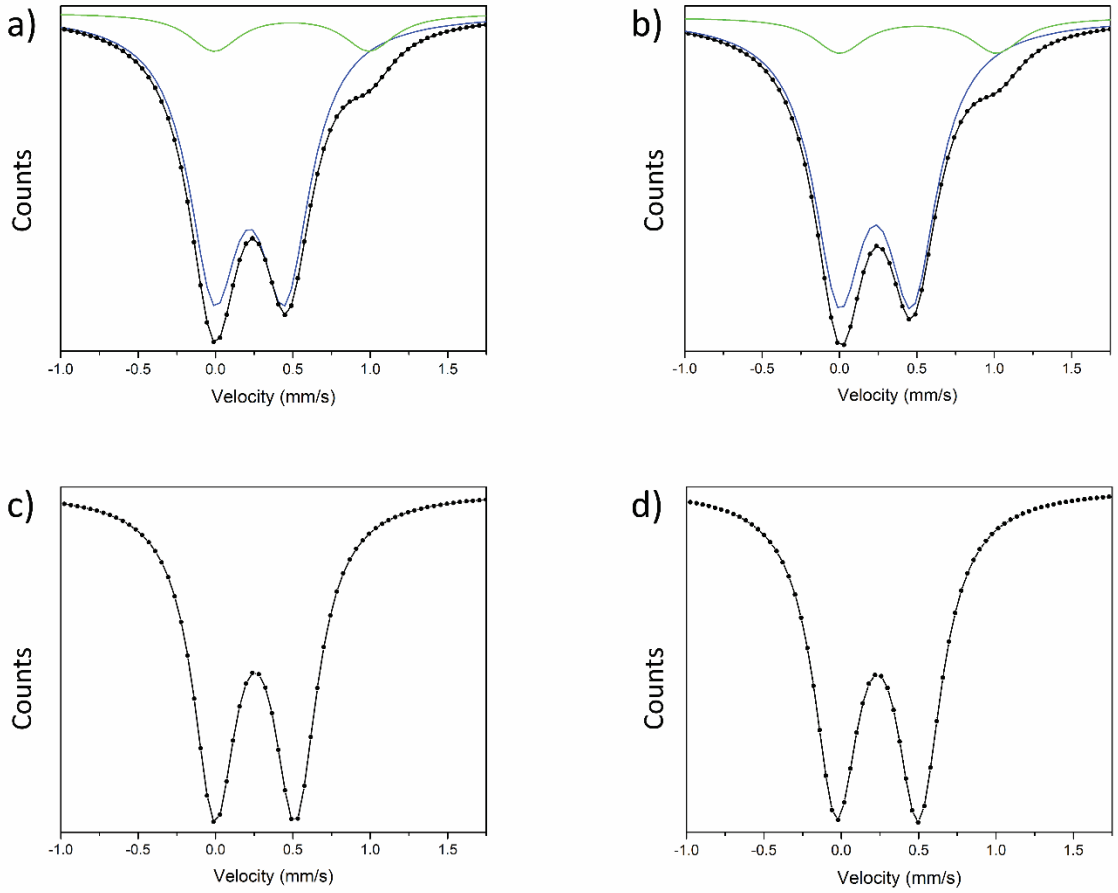

Fig. 3. Mossbauer spectra of BMFT with Fe:Mn ratios of a) 1:2 b) 1:1 c) 2:1 d) 3:1

Compound Fe:Mn Ratio	Fe(O.S.)	O_h:T_d
1:2	III	6.8:1
1:1	III	7.2:1
2:1	III	1:0
3:1	III	1:0

Table 2. Fe oxidation state and coordination ratio (octahedral compared to tetrahedral) obtained using Mossbauer spectroscopy.

The experimental curves for Fig 3. (a) and (b) appear to contain convoluted peaks, made clear by the shoulder at ~1.0 mm/s. This is indicative of the presence of Fe in more than one type of coordination environment. It was therefore determined that an experimental fitting for peak deconvolution was necessary for these two samples, and is shown in Fig. 3(a) and (b), represented by blue and green lines, which correspond to octahedral and tetrahedral coordinated iron respectively.[39] The isomer shift for octahedral iron is 0.239 mm/s, and the quadrupole splitting is 0.490 mm/s; the IS and QS for the tetrahedrally coordinated iron is 0.461 mm/s and 1.00 mm/s respectively. The observed IS and QS fit into the range for Fe(III). Fig. 3(c) and (d) show only one set of peaks corresponding to an octahedral environment. It was concluded that the BMFT compounds have Fe(III) present in both octahedral and tetrahedral environments for Fe:Mn ratios of 1:2 and 1:1, and only octahedral for 2:1 and 3:1 ratios. The possibility of an impurity iron oxide phase was considered unlikely, due to lack of evidence in the XRD pattern. The presence of amorphous Fe_xO_y was also considered unlikely, given the crystallization temperatures involved. Further, the proposition of lattice Fe substitution is highly compelling, from the EDS. Further, increasing the amount of Fe substitution appears to eliminate the presence of tetrahedral Fe: at Fe:Mn ratios of 2:1 and 3:1 (with increased amounts of Fe) only octahedral Fe(III) is present within the compound. Therefore, we conclude that Fe has substituted into the framework and has the possibility of occupying more than one coordination site, depending on the precursor ratio used initially.

3.3 Magnetic Characterization

Magnetization-Temperature and Magnetization-Field (M-T and M-H) curves were obtained using a magnetic properties measurement system (MPMS, Quantum Design) at the Center for Nanophase Materials Science (CNMS), Oak Ridge National Lab (ORNL).

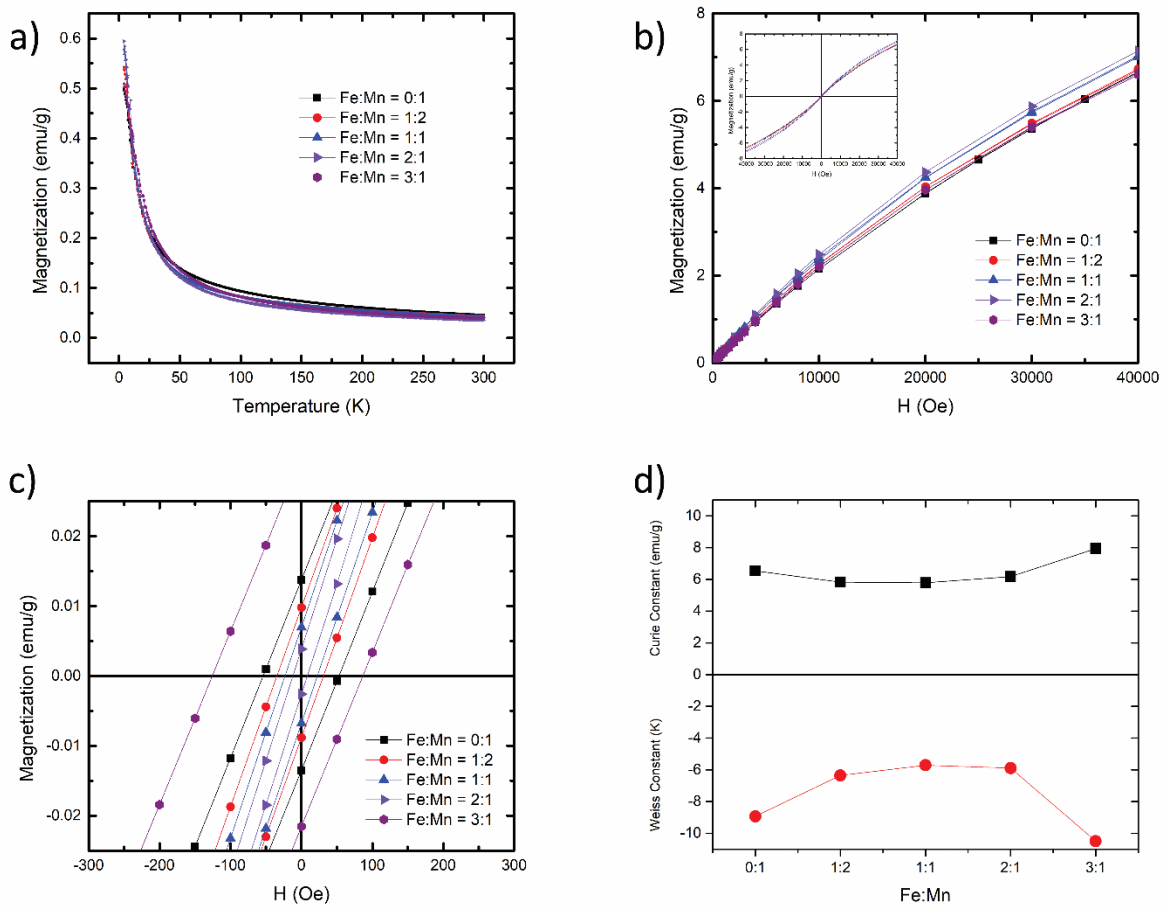

Fig. 4. (a) M-T field cooling (FC) curve with H = 2 kOe. (b) M-H curve taken at 5 K, showing quadrant I; inset showing quadrants I - IV. (c) M-H curve showing M_R and coercivity at 5 K. d) Curie and Weiss constants vs Fe:Mn ratio.

The M-T FC/ZFC curve is shown in Fig. 4(a). Evidence for long range antiferromagnetic ordering is not so apparent from this plot, suggesting paramagnetic behavior, attributed to the nanoscale nature of the compounds and a concurrent large number of surface spins, that likely obscures the observation of any ordering. However, further analysis of the M-H data provides support for antiferromagnetic behavior at low temperatures. The M-H curve, obtained at 5 K and 0 – 40 kOe (Fig. 4 (b)), shows that increasing Fe increases the magnetization (up to Fe:Mn 2:1) until a critical threshold, upon which the magnetization decreases, towards becoming a similar value (in the case of Fe:Mn 3:1) to that of the parent compound. This is henceforth referred to as the magnetic inflection point. Fig. 4 (c) depicts a smaller range of the M-H curves, showing details of the coercivities and remanent magnetizations. The remanent magnetization (M_R)

initially decreased upon addition of iron. However, upon reaching twice the amount of iron as manganese (Fe:Mn = 2:1) this trend reverses and reaches a maximum in the 3:1 compound. In addition, the inflection point brings asymmetry in the hysteresis, indicating there are competing magnetic interactions taking place within the compounds. One explanation for the observation of competing magnetic interactions is the nanoscale effect of surface spins that gives rise to a dominating paramagnetism, versus the tendency toward antiferromagnetic ordering within the interior of the nanocrystal. The magnetic inflection point is noticeable in the calculated constants based upon the Curie-Weiss fit of the M – T curves. Zero-field cooling (ZFC) and field cooling (FC) magnetization curves (M – T) were obtained at a magnetic field of 2 kOe. FC curves are displayed in Fig. 4 (a) for BMT and its variants. ZFC curves are omitted for clarity, as both ZFC and FC converge for the entirety of the temperature range. The most notable difference between BMT and its iron variants occurs at very low temperature readings. As the Fe quantity is increased, maximum magnetization increases. This may be due to the increase in electrons from each atom exchanged within the system. As the thermal motion of the electrons is reduced, the overall magnetization increases proportionally to the number of electrons (equivalent to Fe atoms) added. However, the compound with the most iron (Fe:Mn = 3:1) does not follow this trend. An asymmetric hysteresis curve is seen for this compound in Fig. 4 (c). Asymmetry often arises from competing magnetic phases, which will often lead to a change in the magnetization, depending on the polarity of applied field.

Compound Mn:Fe Ratio	Curie Constant (C)	*b*	Weiss constant (θ)	Effective Magnetic moment (μ_B)	M_R/M_{4T} ($*10^{-3}$)	Coercivity (Oe)
0:1	6.5	0.029	-8.9	4.3	1.9	53
1:2	5.8	0.026	-6.4	4.1	1.5	33
1:1	5.8	0.026	-5.7	4.1	1.0	22
2:1	6.2	0.016	-5.9	4.2	0.6	-12,8.4
3:1	7.9	0.012	-10.5	4.8	-3.2,4.7	-125,87

Table 3. Calculated and fitted values for all synthesized compounds.

To further explore the phenomenon of the inflection point, the Curie and Weiss constants and calculated effective magnetic moments for each compound were obtained (Table 3). The Curie-Weiss fit was based on the equation $X = C/(T-\theta) + b$, where X is the magnetic susceptibility (magnetization), C is the Curie constant, θ is the Weiss constant, T is the temperature in Kelvin, and *b* is a fitting parameter. Fig. 4 (d) reveals the Curie and Weiss constant values increase for increasing Fe:Mn ratios. However, at a Fe:Mn ratio of 2:1 (the magnetic inflection point) the trend reverses. The Weiss constant generally allows for insight into the short-range magnetic interactions within the compound. Here, the Weiss constant values are indicative of antiferromagnetic behavior up to Fe:Mn 2:1. Thereafter, a transition from antiferromagnetic to paramagnetic short-range interactions is likely, consistent with previous evidence of antiferromagnetic order in BMT-134, observed for slightly different sintering conditions ($BaMnTi_4O_{14+\delta}$, $\delta = 0.25$). However, after this point, the Weiss constant begins to decrease and reaches its highest absolute value in BMFT - 3:1. The calculated effective magnetic moments for each compound can be seen in Table 3, column 5. The parent compound has an effective magnetic moment of 4.3 μ_B which closely matches the previously reported value.[16] The changing effective magnetic moment can be explained by the coordination environments of tetrahedral or octahedral Fe in the crystal lattice. An asymmetry occurs in the magnetic hysteresis as is shown in Fig. 4 (c) beginning with BMFT - 2:1. The 2:1 and 3:1 ratio compounds have two separate and asymmetric values for coercivity, which are shown in the last two rows and columns of Table 3. The hysteresis loops for both compounds are biased towards a negative external magnetic field. Generally, asymmetry in hysteresis shows competition between magnetic phases within a single compound. Mossbauer measurements appear to show that BMFT compounds with less iron have Fe(III) in both tetrahedral and octahedral environments, and that both BMFT - 2:1 and BMFT - 3:1 compounds contain only Fe(III) in octahedral environments, which makes the most sense of the hollandite structure. This observation, along with the calculated effective magnetic moments, points to a change in the orbital splitting coordination geometry (crystal field splitting) of the iron. Tetrahedral iron is generally high spin due to its low Δ_t and Fe(III) in this geometry has a theoretical magnetic moment of 5.92 μ_B. This alone would not explain the value of 5.6 μ_B which is the effective magnetic moment of the 2:1 ratio compound. However, there is also octahedral iron present in a low spin configuration which would have a theoretical magnetic moment of 1.73 μ_B. Therefore, the overall magnetic moment could be attributed to a spin configuration contributions from Fe in both T_d and O_h environments.

3.4 Impedance Analysis

Impedance spectroscopy (IS) is a powerful, non-destructive tool for the investigation of dielectric materials and can help correlate the structural and electrical characteristics of nanocrystalline materials as a function of frequency.[40] It can also help identify electrical processes within the system that contribute to the total dielectric behavior. Previously, for nanocrystal (20-50nm) powders prepared at 700°C of BFT-134 we observed giant permittivity at low frequency, and an effective permittivity of 200 at higher frequencies (> 1MHz) which was concluded to be close to the intrinsic value.[16] Giant or colossal dielectric constants are in possession of real values of the permittivity > 10^3, with observations of up to 10^4/10^5 (depending on frequency). In the case of $CaCu_{3-x}Ti_4O_{12}$, including CCTO, very large differences in the real permittivity values have been observed, ranging from 2000-12000 if x is varied from 3 to 2.85, and that the behavior is best explained by thinking of CCTO as possessing a combination of semiconductive and dielectric properties.[41] However it is well known that ceramic permittivity values at low frequency depend greatly on processing conditions that influence grain size, grain boundaries and additional compositional features created during processing that are not necessarily intrinsic to the chemical structure of the compound. Large permittivity values are relevant for devices but other factors, such as breakdown strength, must also be taken into consideration for electronics or energy storage applications.[42–44] In order to assess the dielectric properties, and the ability to prepare device-type configurations, pressed pellet capacitors of each compound were fabricated and sintered to 1000°C. The use of a polymer filler, while attractive for nanocomposite design[45] was ruled out in order that the intrinsic properties of the ceramic BMFT material could be directly contrasted. It is well known that nanostructured ceramic materials with high amounts of surface area, porosity even when compressed, and defects (such as oxygen vacancies) may suffer from interfacial effects such as contact resistance between electrode and oxide. While these features all contribute to the effective permittivity of the material, direct comparisons between varying concentrations of Fe remained feasible. A typical SEM micrograph showing the texture of the pressed BMFT sample, showing a particle size in the range 100-300nm, is shown in the supporting information (Fig. S3). The frequency dependent behavior of the effective permittivity, ε_{eff}, and dissipation loss (tan δ) was obtained for all compounds (Fig. 5). At low frequencies (100 Hz – 1 kHz), large values of ε_{eff} range significantly as a function of Fe content, from 1600 (0:1) down to ~150 (BMFT 3:1). In the 100 kHz-1MHz region, the values decrease and converge towards values between 100-200, The recorded ε_{eff} values (See also supplementary Fig S2, Table S2) at 1MHz are: 110 (BMFT 3:1); 138 (2:1);

157(1:1); 167(1:2) and 206(0:1, BMT). Above 1 MHz a convergence to an intrinsic value due to composition dependent ionic behavior of the compound is observed. The permittivity of nanotextured ceramic materials are in general very sensitive to frequency, due to a potential combination of space charge, interfacial grain boundary effects and intrinsic conductivity (conduction band electrons) of the material. Interfacial polarization heavily influences permittivity, especially at lower frequencies, known, for example, to occur at interfaces between materials with large disparities in permittivity.[46,47] Despite all of these extrinsic factors, the effect of Fe doping is clearly observed. The effective permittivity, ε_{eff} , generally decreases with increasing Fe doping (BMFT - 1:2, - 1:1, 2:1). In the case of highest Fe concentration (BMFT – 3:1) higher values of ε_{eff} are noted < 1kHz, falling to the lowest value (> 1 MHz) of 110. The Fe:Mn ratio appears to greatly affect ε_{eff} both in the lower frequency region (<10kHz) and higher frequency region. To help explain this observation we draw from two areas of the literature: the established topic of dielectric relaxation phenomena in insulating materials, combined with the well-studied, yet lesser formulated topic of internal barrier layer capacitance in giant dielectric materials.

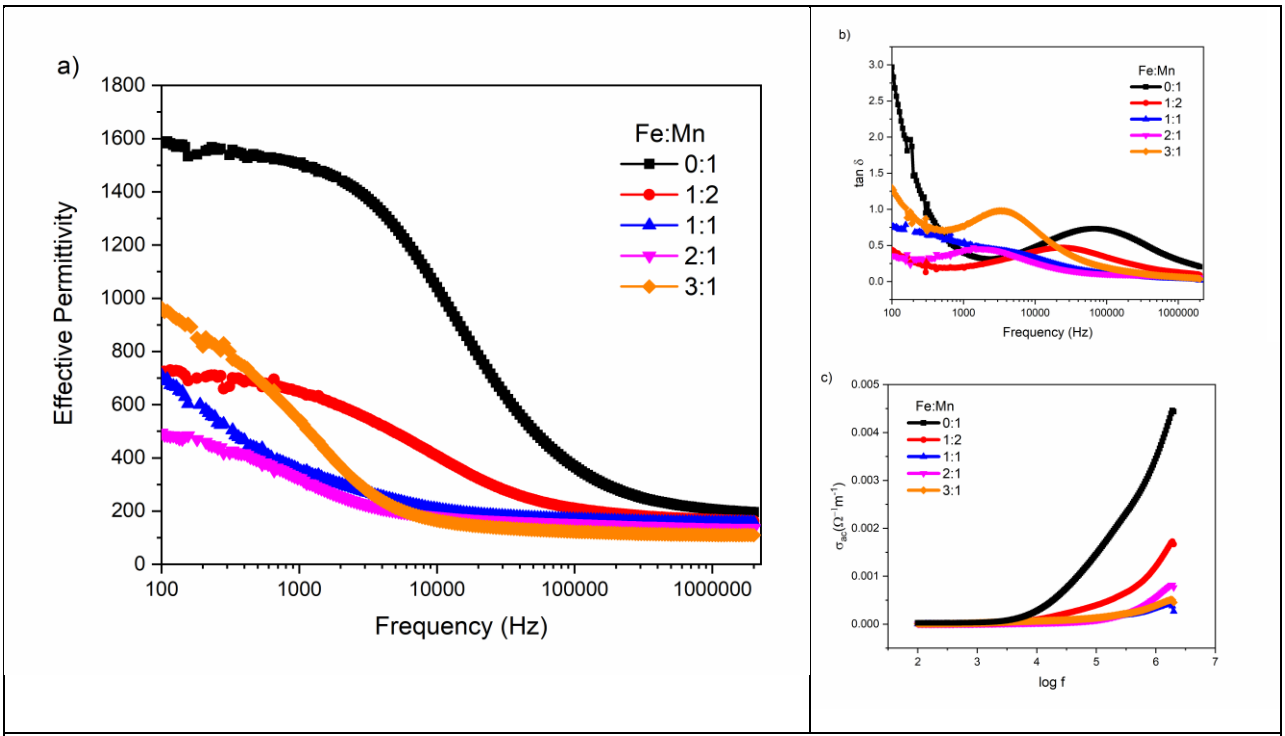

Figure 5. Effective permittivity vs frequency and impedance analysis for the series of BMFT samples (0:1 to to 3:1). Frequency range is 100 Hz to 2 MHz. (a) Effective permittivity vs frequency; (b) dissipation factor (tan δ) vs frequency; (c) ac conductivity (σ_{ac}) vs $\log_{10}$(frequency).

The polarization mechanisms in the low frequency region arise from interfacial (Maxwell-Wagner-Sillars) and additional ionic space-charge effects.[46,47] The ε_{eff} for this region is therefore considered to be dependent on the texture of the pellet and interface between electrode and pellet; and the intrinsic behavior of the BMFT is only one of several contributions. In giant dielectric constant materials, much work has gone towards understanding the cause of unusually high values of ε_{eff}. Internal Barrier Layer Capacitance (IBLC) is an effect that produces very large permittivity values that tend to plateau as a function of frequency and temperature in the 1-100 kHz regime.[33,48–50] It can be thought of as an unintentional barrier layer capacitance (BLC) that occurs naturally as a consequence of the materials internal structure, when induced to form a micro(nano)structured film or pellet. A large capacitive effect results, due to the formation of depletion layers at grain boundaries or the formation of Schottky diodes at the sample/metallic contact interface. While extrinsic effects are the likely explanation,[51] intrinsic effects, such as relaxing defects have also been proposed because of the persistent observation of giant permittivity values even in single or twinned crystal CCTO.[49,52] In industry a strategy exists to create BLC through conductive core/insulating shell grains. The surface or grain boundaries of the dielectric are annealed in the presence of oxidizing agents (e.g. MnO) to produce thin resistive layers. The goal is to create high energy density capacitors. IBCL is contrasted with ferroelectric or relaxor materials that deliver high permittivity, due to displacive ionic and polarization contributions. IBLC is largely attributed to space charge Maxwell-Wagner-Sillars contributions and a concurrent dielectric relaxation.[53] Mobile charge carriers discharge the capacitance (unwanted), but if they are somehow confined to the domain length of the grain they can, in theory, contribute to capacitance without contributing to loss. In practice this is very hard to achieve. Grain size, oxygen deficiency and contacts will all greatly affect the magnitude of the IBCL effect, in terms of permittivity values and loss.[33] The result in most cases is that at low frequencies, ε' is dominated by the extrinsic contact capacitance, which usually is much higher than the intrinsic bulk capacitance. With increasing frequency, the contact capacitor becomes shorted and the intrinsic response is detected.[53]

In the BMFT system, the permittivity values of Fe doped samples are large, 10^2-10^3, while the loss tangent values are indicative of mobile charge carriers. At the frequency range 100Hz – 100kHz we attribute the large value of permittivity to be due to Maxwell-Wagner-Sillars contributions of the type observed for IBLC, and note that the role of Mn in IBLC is much more

pronounced, suggesting that Mn (more than Fe) can switch between a more semiconductive behavior to a highly resistive behavior at the grain boundary. Furthermore, processing conditions greatly affect the size of the dielectric constant at low frequencies. Porosity within the sample is also known to cause a microcapacitance effect. Due to the disparity in dielectric constant between filler (the pelletized nanoparticles) and the matrix (the air gaps between the particles, $\varepsilon_r = 1$), the pellet can be thought of as a mixture of 'micro-capacitors' connected in series and in parallel, separated by insulating grain boundaries.[54] A large disparity in permittivity between filler and matrix is also known to be the cause of inhomogeneity in the electric field within the composites, lowering breakdown strength, and giving rise to large dissipation values.[55] Overall, the shift in values of ε_{eff} as a function of Fe content is concluded to be only partially from a contribution of ionic polarization in the crystal lattice (such as a change in ferroelectric polarization), since the frequency region is too low to correlate for such an effect.

The dissipation loss characteristics of the BMFT sample set can be described as a series of wavelike plots as a function of frequency, with a dielectric absorption peak distinctive for each BMFT variant. To attempt to interpret this behavior, it is necessary to evaluate the contribution of the mean concentration of mobile charge carriers to the real component of the permittivity. The two fundamental parameters that characterize the dielectric are real permittivity, ε' and its conductivity, σ_{ac}. σ_{ac} (Scm^{-1}) is the ratio of leakage current density (D) to the applied electric field (E). Under ac conditions the appearance of a loss or leakage current is manifest as a phase angle difference δ between the $\underline{D}$ and $\underline{E}$ vectors: tan δ is the phase difference that occurs between the electric displacement current density and the applied electric field. Tan δ is the dielectric loss, also referred to as dissipation loss (DF), dissipation factor or loss tangent. Under ac conditions, dielectric losses arise mainly from the movement of free carriers (electrons and ions), space-charge polarization and dipole orientation, all of which are frequency dependent. The introduction of the complex permittivity is useful to help resolve these contributions: $\varepsilon^* = \varepsilon' - j\varepsilon''$. Since, theoretically, ε^* is also equal to the ratio of dielectric displacement vector $\underline{D}$ to the electric field $\underline{E}$ ($\varepsilon^* = \underline{D}/\underline{E}$), an important relationship between the dielectric loss, tan δ, real/imaginary components of the permittivity, and losses due to conductivity can be reached:

$$tan\delta = \frac{\varepsilon''}{\varepsilon'} = \frac{\sigma_{ac}}{\omega\varepsilon'}$$

Where ω = the angular frequency ($2\pi f$). Since $\sigma_{ac} = \tan\delta.\omega.\varepsilon'$, a plot of σ_{ac} against frequency can be generated to assess the ac conductivity behavior as a function of frequency. Conductivity ($Sm^{-1} = \Omega^{-1}m^{-1}$) vs $\log_{10}$ frequency is shown in Figure 5(c). At low frequency σ_{ac} can be observed to be minimal and frequency independent, and can be assumed to reflect the dc conductivity. At higher frequencies (log f >4) σ_{ac} increases steadily as a function of frequency. In this regime the conductivity is strongly frequency dependent, characteristic for ac conduction. The origin of this conductivity behavior is typically attributed to the hopping of carriers between localized states.[56] Increasing the frequency of the electric field stimulates the hopping mechanism and thus mobility of charge carriers. At lower frequencies the grain boundaries are more effective than grains in electrical conduction hence the hopping between $Mn^{3+/4+}$ and Fe^{3+} ions are bound at lower frequencies, and the material remains more resistive. As the frequency of the applied field increases, the carrier hopping intrinsic to the interior of the grains become more active and promotes the ac conduction mechanism, at which point the grains essentially become less resistive. At 1 MHz, closer to an intrinsic effect, the resistive values drop from 400 kΩcm in the case of the highly doped Fe materials to 80 kΩcm (1:2 BMFT) to 29 kΩcm (0:1 BMT) (See Supplementary figure, S7). It is evident that increasing quantities of Fe^{3+} prevent electric conduction due to hopping, suggesting that hopping predominantly occurs for $Mn^{3+/4}$ ions, and Fe^{3+} serves as a barrier for this effect. In the case of BMT, the mechanism responsible for ferroelectricity was partially attributed to charge ordering between Mn^{3+} and Mn^{4+} neighboring octahedra,[16] which may also reduce electron conductivity, but it is readily concluded that the alteration of the Fe:Mn ratio and concurrent change in electronic configuration from d^3 to d^5, demonstrates a strong effect on conductivity mechanisms (electron hopping) within the material.

4. Conclusions

A sol-gel based nanocrystal nucleation and growth synthesis method (gel-collection) was used to obtain a set of Fe substituted compounds of the form $BaMn_{3-x}Fe_xTi_4O_{14+\delta}$, and the synthesis was proven to have high precursor/product ratio fidelity. The parent compound and Fe substituted analogues were found to be an isostructural hollandite structure (Space group I4/m) but displayed different magnetic and dielectric properties. Incorporation of Fe was identified using energy dispersive X-ray spectroscopy (EDS), and evaluated using Mossbauer spectroscopy. Manganese octahedra within the multiferroic BMT–134 were successfully replaced with Fe, especially up to Fe:Mn 2:1. An inflection point in the magnetization shows a

change in short range electron interaction behavior, giving evidence of an antiferromagnetic to paramagnetic transition. Dielectric characterization demonstrated the addition of iron causes a large effect in the effective permittivity. The recorded ε_{eff} values for BMFT show a convergence (1 MHz) to an intrinsic value ~200, in spite of frequency dependent behavior which is concluded to be a function of the Fe composition level. The permittivity is very sensitive to frequency, due to a potential combination of space charge, interfacial grain boundary effects and intrinsic conductivity (conduction band electrons) of the material. Despite all of these texture-based extrinsic factors, the effect of Fe doping is clearly observed. From the AC Conductivity measurement, it is concluded that increasing quantities of Fe^{3+} prevent electric conduction due to hopping, suggesting that hopping predominantly occurs for $Mn^{3+/4}$ ions, and Fe^{3+} serve as a barrier for this effect. The successful inclusion of an additional transition metal oxide demonstrated here, strongly suggests that additional transition metal (e.g. Ni, Co) or rare earth metal cations, of comparable size and oxidation states might be allowed to intersubstitute into this structure, for additional structure-property control.

Acknowledgements

This work was supported by the National Science Foundation, under NSF DMR award #1461499, and with an additional support from NSF CREST #1547830. S.O. and FP are grateful to AGEP award supplements NSF DMR # 1719250 and #1831127, on behalf of FP. FP and SO are very grateful to both Dr. Jun Ouyang and Dr. Jackie Li for useful discussions regarding dielectric behavior. FP and JL are grateful to Jorge Morales for help with the EM. All magnetic characterization was conducted at the Center for Nanophase Materials Sciences, Oak Ridge National Laboratory, which is a DOE Office of Science User Facility (supported under Project Number CNMS2017-211). S.O. and N.F. thank Ioannis Kymissis and Christine McGinn for assistance with recording the impedance data.

Appendix A. Supplementary data

Supplementary data to this article can be found online at _____. Supplementary data contains information and figures of synthesis products of BMFT, pressed pellets and dissipation. TEM and SEM morphology. 3D planes corresponding to Miller indices comparing shifts in d-spacing are also presented.

References

(1) Eerenstein, W.; Mathur, N. D.; Scott, J. F. Multiferroic and Magnetoelectric Materials.

Nature **2006**, *442*, 759–765.

(2) Spaldin, N. A. Multiferroics: Past, Present, and Future. *MRS Bull.* **2017**, *42*, 385–389.

(3) Fiebig, M.; Lottermoser, T.; Meier, D.; Trassin, M. The Evolution of Multiferroics. *Nat. Rev. Mater.* **2016**, *1*, 1–14.

(4) Kalinin, S. V.; Spaldin, N. A. Functional Ion Defects in Transition Metal Oxides. *Science (80-.).* **2013**, *341*, 858–859.

(5) Seidel, J.; Martin, L. W.; He, Q.; Zhan, Q.; Chu, Y. H.; Rother, A.; Hawkridge, M. E.; Maksymovych, P.; Yu, P.; Gajek, M.; *et al.* Conduction at Domain Walls in Oxide Multiferroics. *Nat. Mater.* **2009**, *8*, 229–234.

(6) Spanier, J. E.; Kolpak, A. M.; Urban, J. J.; Grinberg, I.; Ouyang, L.; Yun, W. S.; Rappe, A. M.; Park, H. Ferroelectric Phase Transition in Individual Single-Crystalline $BaTiO_3$ Nanowires. *Nano Lett.* **2006**, *6*, 735–739.

(7) Smith, M. B.; Page, K.; Siegrist, T.; Redmond, P. L.; Walter, E. C.; Seshadri, R.; Brus, L. E.; Steigerwald, M. L. Crystal Structure and the Paraelectric-to-Ferroelectric Phase Transition of Nanoscale $BaTiO_3$. *J. Am. Chem. Soc.* **2008**, *130*, 6955–6963.

(8) Page, K.; Proffen, T.; Niederberger, M.; Seshadri, R. Probing Local Dipoles and Ligand Structure in $BaTiO_3$ Nanoparticles. *Chem. Mater.* **2010**, *22*, 4386–4391.

(9) Polking, M. J.; Han, M. G.; Yourdkhani, A.; Petkov, V.; Kisielowski, C. F.; Volkov, V. V.; Zhu, Y.; Caruntu, G.; Paul Alivisatos, A.; Ramesh, R. Ferroelectric Order in Individual Nanometre-Scale Crystals. *Nat. Mater.* **2012**, *11*, 700–709.

(10) Shi, C.; Billinge, S. J. L.; Puma, E.; Bang, S. H.; Bean, N. J. H.; De Sugny, J. C.; Gambee, R. G.; Haskell, R. C.; Hightower, A.; Monson, T. C. Barium Titanate Nanoparticles: Short-Range Lattice Distortions with Long-Range Cubic Order. *Phys. Rev. B* **2018**, *98*, 1–13.

(11) Braun, E.; Keren, K. Topological Effects in Nanomagnetism. *Adv. Phys.* **2012**, *61*, 1–116.

(12) Fitzsimmons, M. R.; Bader, S. D.; Borchers, J. A.; Felcher, G. P.; Furdyna, J. K.; Hoffmann, A.; Kortright, J. B.; Schuller, I. K.; Schulthess, T. C.; Sinha, S. K.; *et al.* Neutron Scattering Studies of Nanomagnetism and Artificially Structured Materials. *J. Magn. Magn. Mater.* **2004**, *271*, 103–146.

(13) Fernández-Pacheco, A.; Streubel, R.; Fruchart, O.; Hertel, R.; Fischer, P.; Cowburn, R. P. Three-Dimensional Nanomagnetism. *Nat. Commun.* **2017**, *8*, 15756.

(14) Leland, E. S.; Kinget, P. R.; Kymissis, I.; Steingart, D.; Sanders, S. R.; O'Brien, S. Nanocomposite Capacitors in Power Electronics and Multiferroics. *IEEE Nanotechnol. Mag.* **2018**, *13*, 1–1.

(15) Miura, H. The Crystal Structure of Hollandite. *Mineral. J.* **1986**, *13*, 119–129.

(16) Liu, S.; Akbashev, A. R.; Yang, X.; Liu, X.; Li, W.; Zhao, L.; Li, X.; Couzis, A.; Han, M.-G.; Zhu, Y.; *et al.* Hollandites as a New Class of Multiferroics. *Sci. Rep.* **2014**, *4*, 6203.

(17) Hossain, M. E.; Liu, S.; O'Brien, S.; Li, J. Frequency-Dependent Ferroelectric Behavior of $BaMn_3Ti_4O_{14.25}$ at Room Temperature. *Appl. Phys. Lett.* **2015**, *107*, 032904.

(18) Abrahams, S. C. Systematic Prediction of New Ferroelectric Inorganic Materials in Point Group 6. *Acta Crystallogr. Sect. B* **1990**, *46*, 311–324.

(19) Foley, J. A.; Hughes, J. M.; Drexler, J. W. Redledgeite, $Ba_x[Cr,Fe,V]_{2x}Ti_{8-2x}O_{16}$, the I4/m Structure and Elucidation of the Sequence of Tunnel Ba Cations. *Can. Mineral.* **1997**, *35*, 1531–1534.

(20) Sinclair, W.; McLaughlin, G. M.; Ringwood, A. E. The Structure and Chemistry of a Barium-Titanate Hollandite- Type Phase. *Acta Crystallogr. Sect. B-Structural Sci.* **1980**, *36*, 2913–2918.

(21) Leinekugel-le-Cocq, A. Y.; Deniard, P.; Jobic, S.; Cerny, R.; Bart, F.; Emerich, H. Synthesis and Characterization of Hollandite-Type Material Intended for the Specific Containment of Radioactive Cesium. *J. Solid State Chem.* **2006**, *179*, 3196–3208.

(22) Hao, Y. N.; Bi, K.; O'Brien, S.; Wang, X. X.; Lombardi, J.; Pearsall, F.; Li, W. L.; Lei, M.; Wu, Y.; Li, L. T. Interface Structure, Precursor Rheology and Dielectric Properties of $BaTiO_3$/PVDF-Hfp Nanocomposite Films Prepared from Colloidal Perovskite Nanoparticles. *RSC Adv.* **2017**, *7*, 32886–32892.

(23) Liu, S.; Zhang, H.; Sviridov, L.; Huang, L.; Liu, X.; Samson, J.; Akins, D.; Li, J.; O'Brien, S. Comprehensive Dielectric Performance of Bismuth Acceptor Doped $BaTiO_3$ Based Nanocrystal Thin Film Capacitors. *J. Mater. Chem.* **2012**, *22*, 21862–21870.

(24) Liu, S.; Huang, L.; Li, W.; Liu, X.; Jing, S.; Li, J.; O'Brien, S. Green and Scalable

Production of Colloidal Perovskite Nanocrystals and Transparent Sols by a Controlled Self-Collection Process. *Nanoscale* **2015**, *7*, 11766–11776.

(25) Lombardi, J.; Pearsall, F.; Li, W.; O'Brien, S. Synthesis and Dielectric Properties of Nanocrystalline Oxide Perovskites, $[KNbO_3]_{1-x}[BaNi_{0.5}Nb_{0.5}O_{3-\delta}]_x$, Derived from Potassium Niobate KNbO3 by Gel Collection. *J. Mater. Chem. C* **2016**, *4*, 7989–7998.

(26) Huang, L.; Jia, Z.; Kymissis, L.; O'Brien, S. High K Capacitors and OFET Gate Dielectrics from Self-Assembled $BaTiO_3$ and $(Ba,Sr)TiO_3$ Nanocrystals in the Superparaelectric Limit. *Adv. Funct. Mater.* **2010**, *20*, 554–560.

(27) Schwartz, R. W. Chemical Solution Deposition of Perovskite Thin Films. *Chem. Mater.* **1997**, *4756*, 2325–2340.

(28) O'Brien, S.; Brus, L.; Murray, C. B. Synthesis of Monodisperse Nanoparticles of Barium Titanate: Toward a Generalized Strategy of Oxide Nanoparticle Synthesis. *J. Am. Chem. Soc.* **2001**, *123*, 12085–12086.

(29) Niederberger, M. Nonaqueous Sol-Gel Routes to Metal Oxide Nanoparticles. *Acc. Chem. Res.* **2007**, *40*, 793–800.

(30) Fan, H.; Li, H.; Liu, B.; Lu, Y.; Xie, T.; Wang, D. Photoinduced Charge Transfer Properties and Photocatalytic Activity in Bi2O3/BaTiO3 Composite Photocatalyst. *ACS Appl. Mater. Interfaces* **2012**, *4*, 4853–4857.

(31) Pearsall, F. A.; Lombardi, J.; O'Brien, S. Monomer Derived Poly(Furfuryl)/$BaTiO_3$ 0-3 Nanocomposite Capacitors: Maximization of the Effective Permittivity Through Control at the Interface. *ACS Appl. Mater. Interfaces* **2017**, *9*, 40324–40332.

(32) Liu, S.; Huang, L.; Li, W.; Liu, X.; Jing, S.; Li, J.; O'Brien, S. Green and Scalable Production of Colloidal Perovskite Nanocrystals and Transparent Sols by a Controlled Self-Collection Process. *Nanoscale* **2015**, *7*, 11766–11776.

(33) Kuang, X.; Bridges, C.; Allix, M.; Claridge, J. B.; Hughes, H.; Rosseinsky, M. J. Internal Barrier Layer Capacitance Effect in Hexagonal Perovskite $Ba_4YMn_3O_{11.5}$ Ceramics. *Chem. Mater.* **2006**, *18*, 5130–5136.

(34) Fujimoto, K.; Yamakawa, C.; Ito, S. Crystal Growth and Structure Refinement of Hollandite-Type $K_{1.59}Ga_{1.59}Ti_{6.41}O_{16}$. *Solid State Ionics* **2011**, *184*, 74–77.

(35) Wu, C.; Wei, H.; Ning, B.; Yang, J.; Xie, Y. New Phase Hollandite-Type VOOH Quadrangular Nanorods: A New Smart Electrical Switch Material. *Chem. Commun.* **2010**, *46*, 1845–1847.

(36) Ishiwata, S.; Bos, J. W. G.; Huang, Q.; Cava, R. J. Structure and Magnetic Properties of Hollandite $Ba_{1.2}Mn_8O_{16}$. *J. Phys. Condens. Matter* **2006**, *18*, 3745–3752.

(37) Gatehouse, B. M.; Jones, G. C.; Pring, A.; Symes, R. F. The Chemistry and Structure of Redledgeite. *Mineral. Mag.* **1986**, *50*, 709–715.

(38) Gol'danskiĭ, V. I.; Herber, R. H. *Chemical Applications of Mössbauer Spectroscopy.*; Academic Press: New York, 1968.

(39) Katayama, T.; Yasui, S.; Osakabe, T.; Hamasaki, Y.; Itoh, M. Ferrimagnetism and Ferroelectricity in Cr-Substituted $GaFeO_3$ Epitaxial Films. *Chem. Mater.* **2018**, *30*, 1436–1441.

(40) Dorf, R. C. *The Electrical Engineering Handbook*; Richard C. Dorf, Ed.; Elsevier Academic Press: London, 2000.

(41) Ribeiro, W. C.; Joanni, E.; Savu, R.; Bueno, P. R. Nanoscale Effects and Polaronic Relaxation in $CaCu_3Ti_4O_{12}$ Compounds. *Solid State Commun.* **2011**, *151*, 173–176.

(42) Aparicio, M.; Jitianu, A.; Lisa C Klein. *Sol-Gel Processing for Conventional and Alternative Energy*; 2012.

(43) Wang, Y.; Jie, W.; Yang, C.; Wei, X.; Hao, J. Colossal Permittivity Materials as Superior Dielectrics for Diverse Applications. *Adv. Funct. Mater.* **2019**, *29*, 1–27.

(44) Roscow, J. I.; Bowen, C. R.; Almond, D. P. Breakdown in the Case for Materials with Giant Permittivity? *ACS Energy Lett.* **2017**, *2*, 2264–2269.

(45) Pearsall, F. A.; Lombardi, J.; Farahmand, N.; Tassel, B. van; Leland, E. S.; Huang, L.; Liu, S.; Yang, S.; Le, C.; Kymissis, I.; *et al.* Polymer-Nanocrystal Nanocomposites: Device Concepts in Capacitors and Multiferroics. *IEEE Trans. Nanotechnol.* **2019**, *19*, 255–268.

(46) Sihvola, A. Mixing Rules with Complex Dielectric Coefficients. *Subsurface Sensing Technologies and Applications*, 2000, *1*, 393–415.

(47) Sihvola, A. H.; Institution of, E. E. *Electromagnetic Mixing Formulas and Applications*;

Electromagnetics and Radar Series; Institution of Electrical Engineers, 1999.

(48) Adams, T. B.; Sinclair, D. C.; West, A. R. Giant Barrier Layer Capacitance Effects in $CaCu_3Ti_4O_{12}$ Ceramics. *Adv. Mater.* **2002**, *14*, 1321–1323.

(49) Subramanian, M. A.; Li, D.; Duan, N.; Reisner, B. A.; Sleight, A. W. High Dielectric Constant in $ACu_3Ti_4O_{12}$ and $ACu_3Ti_3FeO_{12}$ Phases. *J. Solid State Chem.* **2000**, *151*, 323–325.

(50) Renner, B.; Lunkenheimer, P.; Schetter, M.; Loidl, A.; Reller, A.; Ebbinghaus, S. G. Dielectric Behavior of Copper Tantalum Oxide. *J. Appl. Phys.* **2004**, *96*, 4400–4404.

(51) Sinclair, D. C.; Adams, T. B.; Morrison, F. D.; West, A. R. $CaCu_3Ti_4O_{12}$: One-Step Internal Barrier Layer Capacitor. *Appl. Phys. Lett.* **2002**, *80*, 2153–2155.

(52) Homes, C. C.; Vogt, T.; Shapiro, S. M.; Wakimoto, S.; Ramirez, A. P. Optical Response of High-Dielectric-Constant Perovskite-Related Oxide. *Science (80-.).* **2001**, *293*, 673–676.

(53) Lunkenheimer, P.; Götzfried, T.; Fichtl, R.; Weber, S.; Rudolf, T.; Loidl, A.; Reller, A.; Ebbinghaus, S. G. Apparent Giant Dielectric Constants, Dielectric Relaxation, and Ac-Conductivity of Hexagonal Perovskites $La_{1.2}Sr_{2.7}BO_{7.33}$ (B=Ru, Ir). *J. Solid State Chem.* **2006**, *179*, 3965–3973.

(54) Yang, Q.; Zhang, W.; Yuan, M.; Kang, L.; Feng, J.; Pan, W.; Ouyang, J. Preparation and Characterization of Self-Assembled Percolative $BaTiO_3$–$CoFe_2O_4$ Nanocomposites via Magnetron Co-Sputtering. *Sci. Technol. Adv. Mater.* **2014**, *15*, 025003.

(55) Prateek; Thakur, V. K.; Gupta, R. K. Recent Progress on Ferroelectric Polymer-Based Nanocomposites for High Energy Density Capacitors: Synthesis, Dielectric Properties, and Future Aspects. *Chem. Rev.* **2016**, *116*, 4260–4317.

(56) Verma, K.; Kumar, A.; Varshney, D. Dielectric Relaxation Behavior of $A_xCo_{1-x}Fe_2O_4$ (A = Zn, Mg) Mixed Ferrites. *J. Alloys Compd.* **2012**, *526*, 91–97.